AIAA JOURNAL
Vol. 42, No. 7, July 2004

Jet Interaction with a Primary Jet and an Array of Smaller Jets

Valerio Viti,* Scott Wallis,† and Joseph A. Schetz‡
Virginia Polytechnic Institute and State University, Blacksburg, Virginia 24060
Reece Neel§
AeroSoft, Inc., Blacksburg, Virginia 24060
and
R. D. W. Bowersox¶
Texas A&M University, College Station, Texas 77843

A combined experimental–numerical study of the jet interaction flowfield associated with sonic injection of a gas into a turbulent, high-speed crossflow ($M = 4.0$) was conducted with an innovative configuration for jet-thruster applications. This configuration consists of a sonic primary jet, flanked by arrays of smaller secondary sonic injectors that interact with the flowfield created by the primary jet. The mass flow from the small secondary jets ranged from 0.5–1% of that from the primary jet. Pressure sensitive paint was used to measure the pressure field acting on the surface. Forces and moments acting on the flat plate were quantified by integration of the pressure field. Schlieren photographs were used to analyze the main flow features generated by the jet interaction. The numerical solution used the Reynolds-averaged Navier–Stokes equations and Wilcox's k–ω turbulence model. The study showed that the main improvement of this configuration was a considerable reduction (by as much as 164%) in the generally undesirable nose-down pitching moment typical of jet-interaction flows. A secondary benefit was a small increase in the normal force by as much as 3%. These two effects were caused by reductions in both the size and intensity of the low-pressure region aft of the primary injector and, in some cases, by an increase in the extent and intensity of the separation region in front of the jet. The location of the secondary injector was not optimized here; it is believed that even larger improvements in the performance can be obtained by strategically locating the secondary injectors.

Nomenclature

A	=	plate area, m^2
a	=	speed of sound, m/s
C_{Fx}	=	axial force coefficient
C_{Fy}	=	normal force coefficient
C_{Mz}	=	pitching moment coefficient
C_p	=	pressure coefficient
D	=	jet diameter, m
F_x	=	axial force, N
F_y	=	normal force, N
H	=	height of the barrel shock from the tunnel floor, m
k	=	turbulent kinetic energy, m^2/s^2
L	=	axial (x) length of plate, m
M	=	Mach number
M_z	=	pitching moment, Nm
P	=	static pressure, Pa
PR	=	pressure ratio ($P_{0,j}/P_\infty$)
Pr	=	Prandtl number, $Pr_{\text{perfect gas}}$, 0.72
P_0	=	total pressure, Pa
Re	=	Reynolds number
T	=	static temperature, K
T_0	=	total temperature, K
t	=	time, s
u, v, w	=	Cartesian velocity components, m/s
x, y, z	=	Cartesian coordinates, m
β	=	angle between the zero-C_p line and the tunnel centerline, deg
γ	=	specific heat ratio, $\gamma_{\text{perfect gas}}$, 1.40
δ	=	boundary-layer thickness, m
ε	=	turbulence dissipation rate, m^2/s^2
θ_1	=	inclination of the bow shock to the tunnel floor, deg
θ_2	=	inclination of the barrel shock to the tunnel floor, deg
λ	=	second bulk viscosity coefficient, Ns/m^2
μ	=	laminar (molecular) viscosity (first bulk viscosity coefficient), Ns/m^2
μ_T	=	turbulent (eddy) viscosity, Ns/m^2
ν	=	kinematic viscosity, m^2/s
ρ	=	density, kg/m^3
τ	=	shear stress, N/m^2
ω	=	turbulent frequency, m^3/s^3

Subscripts

inf	=	freestream condition
j	=	jet condition
jet	=	jet condition
wall	=	wall condition
∞	=	freestream condition
$*$	=	nondimensionalized value

Superscripts

~	=	mean value of Favre-averaged variable
-	=	time-averaged values
$''$	=	fluctuating value of Favre-averaged variable

Received 28 August 2003; revision received 22 January 2004; accepted for publication 10 March 2004.

*Graduate Research Assistant, Department of Aerospace Engineering; currently Postdoctoral Researcher, Department of Mechanical Engineering, University of Kentucky, 210 RGAN Building, Lexington, KY 40506; vviti@uky.edu.

†Graduate Research Assistant; currently Staff Member, SAIC, 1710 SAIC Drive, MacLean, VA 22102.

‡Fred D. Durham Endowed Chair, Department of Aerospace Engineering. Fellow AIAA.

§Research Scientist, 1872 Pratt Drive, Suite 1275.

¶Associate Professor, Department of Aerospace Engineering, 3141 TAMU. Associate Fellow AIAA.

Introduction

THE jet-interaction flowfield produced by a jet exhausting in a crossflow (Figs. 1a and 1b) is a complex problem found in

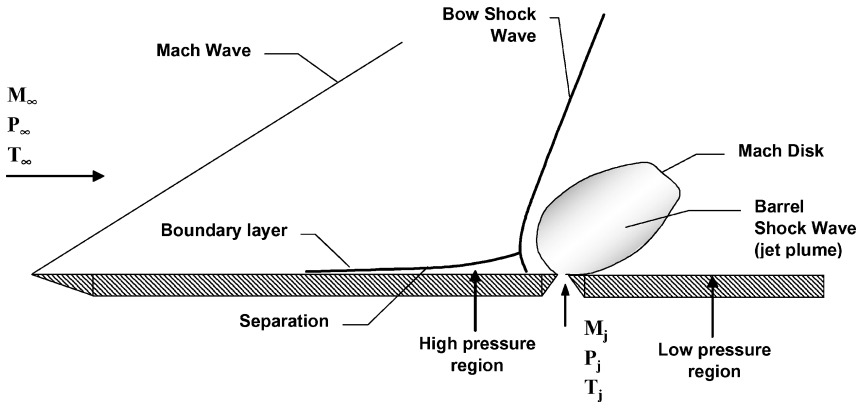

a) Schematic cut along the flowfield centerline, PR = $P_{T,j}/P_{s,\infty}$

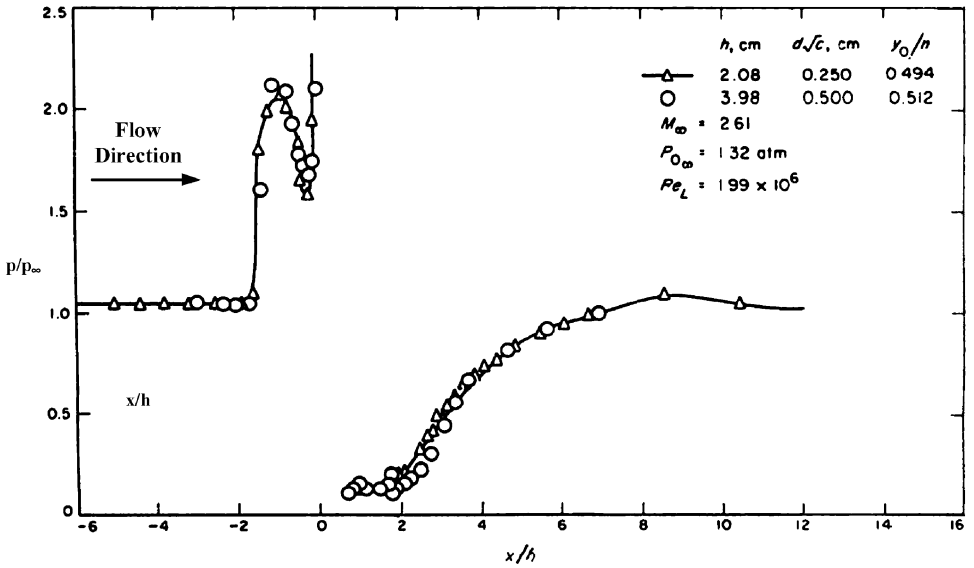

b) Typical pressure distribution along the flowfield centerline for a three-dimensional jet interaction flowfield[2]

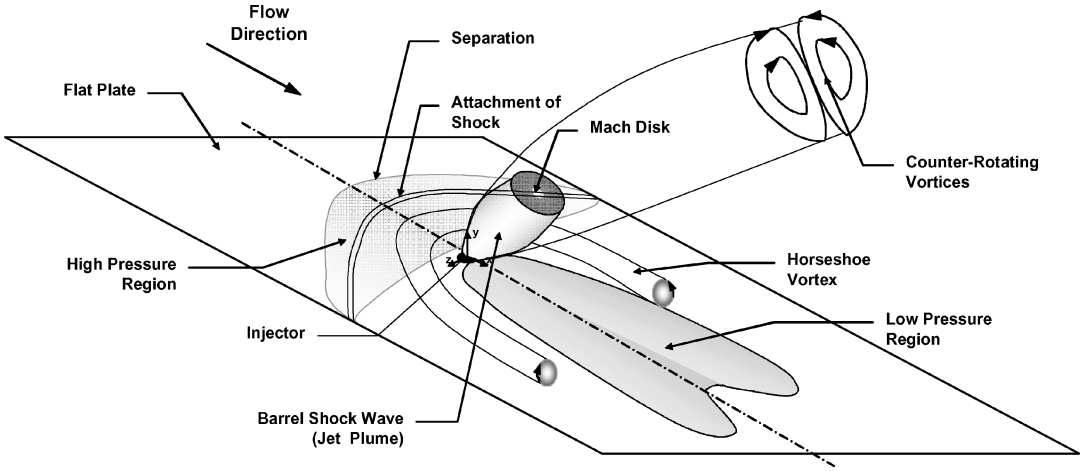

c) Three-dimensional schematic view of the jet interaction problem with a single circular jet normally injecting into a supersonic crossflow

Fig. 1 Sonic jet in a high-speed crossflow.

numerous applications. Reference 1 has a detailed review of the field. Typical applications of the jet-interaction flow range from the very low-speed regime of a chimney plume in a crossflow to the very high-speed cases of scramjet and hypersonic missile control systems.[1]

The basic problem of a gas injected into a crossflow has several variations, depending on the application.[1] Examples of such variables are the yaw and pitch angle of the injector and the flow conditions of the jet (subsonic, sonic, supersonic) and of the freestream (subsonic, supersonic, laminar, turbulent), not to mention the chemical composition of the gases (perfect gas, single or multiple phase, nonreacting mixture, reacting mixture, etc.). The present study focuses on the case of normal injection of a sonic circular jet into a supersonic turbulent crossflow.[1] This configuration is representative of typical reaction control systems installed on hypersonic vehicles such as experimental aircraft, for example, the X-15; reentry vehicles, for example, the space shuttle and future reusable launch systems; and missiles, for example, the national missile defense interceptors or high-altitude surface-to-air missiles (SAMs).

In reaction control systems, normal injection is commonly used because it maximizes the lateral force produced by the thrust of the jet. Two primary mechanisms contribute to the production of the lateral force. The first contribution comes from the thrust of the jet. The second contribution is produced by the complex interaction of the jet with the crossflow. The injected gas acts as an obstruction that produces a shock wave in the primary flow (Fig. 1a). The shock wave produces an adverse pressure gradient, causing boundary-layer separation. The high pressures typical of recirculated flows (as in the pressure plot of Fig. 1b[2]) augment the lateral force produced by the thrust of the jet. Therefore, a jet exhausting into a supersonic crossflow will produce a much larger force than the same jet exhausting into a quiescent medium. However, a large low-pressure region forms aft of the injector (Fig. 1b). This region has two main effects on the forces and moments produced by the jet on the surface. First, the net normal force is decreased because the low pressures act over a large area behind the injector. Second, and perhaps more detrimental, a couple is formed with the high-pressure region ahead of the jet to produce a nose-down moment about the injector. The contribution to the nose-down moment from the low-pressure region is particularly high because, as mentioned earlier, this region extends far aft of the injector, and so its moment arm is relatively large.

The decrease in normal force can be compensated for by an increase in the total thrust of the jet. On the other hand, the nose-down pitching moment cannot be corrected so easily. The nose-down moment must be suppressed or cancelled. An aft thruster will create a nose-up moment. However, this configuration adds complexity and cost, increases the fuel requirements, and complicates packaging.

The disadvantages of double-thruster configurations can be reduced by the design of a single thruster that minimizes or cancels the region of negative pressure aft of the injector. In 1998, a team at Virginia Polytechnic Institute and State University[3] (VT) discovered an interesting feature of multiple-injector configurations. In an array of jets arranged to form an aerodynamic ramp, the influence of the injectors located in the second row of the array was to suppress the area of negative C_p behind the first row of injectors. A study was initiated at VT to determine the feasibility of the use of small, strategically located secondary jets to suppress the low-pressure region. This paper summarizes the results of the combined experimental/numerical study.

In a preliminary numerical study, relatively simple jet-interaction flowfields were simulated. Two laminar cases were simulated.[4,5] Comparisons of the numerical solutions to the experimental results were favorable. The first simulation of a jet-interaction problem with a turbulent boundary layer was that of an experiment by Letko.[6] Following that, a smaller secondary jet was simulated behind the primary jet for the conditions of the original Letko experiment. The numerical results showed that the secondary jet had the desired effect of increasing the normal force on the flat plate and decreasing the nose-down pitching moment. Consequently, a more detailed study that used both experimental and numerical resources available at VT was designed to further investigate the effects of insertion of smaller secondary injectors aft of the primary injector.

Description of the Experiment

For the experiments described in this paper, the primary injector was tested with two pressure ratios: 532 and 620. The tests with a pressure ratio of 620 were used as proof of concept to show qualitatively that a smaller secondary injector could decrease the area of negative C_p aft of the primary injector. Several injector configurations were run with these conditions. On the other hand, only one test with a jet pressure ratio of 532 was run. All tests were run in the VT supersonic wind tunnel, which is of the blowdown type with a working section measuring 23×23 cm. In this setup, the flat surface with the normal injector was mounted flush to the tunnel wall, downstream of the tunnel throat. Complete details of the experimental setup and procedures can be found in Ref. 7.

A developed turbulent boundary layer existed at the leading edge of the flat surface, and the boundary-layer thickness was measured from the schlieren photographs. The fact that the plate was mounted flush to the tunnel floor introduced a weak shock produced by the slight misalignment of the junction between the tunnel floor and the flat plate (Interference shock; Fig. 2). This shock was not included in the numerical simulations, and it could have changed the flow conditions at the injection location, introducing a source of discrepancy between the experimental results and the numerical solution. The flat plate had one primary injector drilled in to its surface and five pairs of secondary injectors drilled behind the primary one. Both the primary and the secondary injectors were converging nozzles drilled through the thickness of the flat plate (Fig. 3).

The secondary injectors were drilled along a straight line on the surface of the plate that formed an angle of 13 deg with the plate, as shown in Fig. 4. This arrangement was selected based on the geometry of the low-pressure region behind a single, sonic jet in a supersonic crossflow taken from experiments in the literature.[2,5,6] The pairs of secondary injectors were identified by a group number: Group 1 is located 1.78 cm behind the primary injector, group 2 is 2.54 cm behind the primary injector, and so on. The plate dimensions are 30.48 cm long and 22.86 cm wide. The nominal flow conditions for the experiments and the numerical computations and the flat plate dimensions are shown in Tables 1–3.

Several pressure orifices were embedded in the surface of the flat plate; however, the detailed pressure field acting on the flat plate was measured and mapped by the use of pressure-sensitive paint (PSP),[8,9] and the pressure taps were used for calibration and for double checking the PSP pressure readings. (See Ref. 7 for details.) There are considered to be three related sources of uncertainty in

Table 1 Flat plate and injector dimensions for the VT experiment

Parameter	Value
Flat plate entry length x_0	7.62 cm
Injector diameter d_j	0.48 cm
$A_{\text{primary}}/A_{\text{secondary}}$	$\cong$100
x_0/d_j	16.0

Table 2 Summary of flow parameters for the cases studied: freestream

	VT Mach 4.0	
Parameter	CFD	Experiment
Gas	Air, perfect gas ($\gamma = 1.40$)	
M_∞	4.0	4.0
$P_{\infty,t}$	1120 kPa	1045 kPa
P_∞	7.1 kPa	6.2 kPa
T_∞	70.3 K	68.8 K
Turbulence model	(Wilcox κ–ω)[10,11]	(Wilcox κ–ω)[10,11]
Inlet δ	1.65 cm	1.65 cm

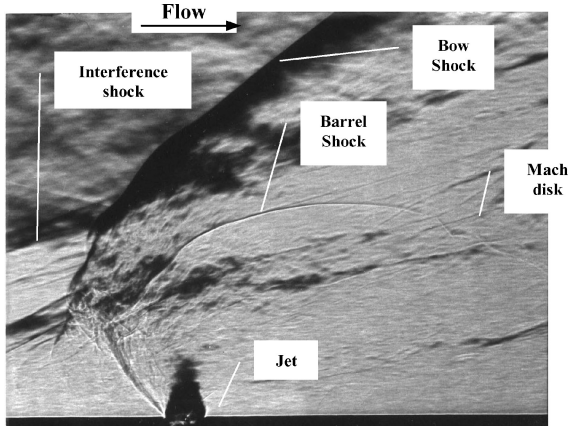

Fig. 2 Schlieren photograph of the flowfield generated by the primary jet only: $M = 4.0$ and PR = 532.

Table 3 Summary of flow parameters for the cases studied: primary and secondary jets

Parameter	CFD	Experiment
Gas	Air, perfect gas ($\gamma = 1.40$)	
M_J	1.0	1.0
$P_{J,t}$	3797 kPa	3835 kPa
P_J	2006 kPa	2026 kPa
T_J	261 K	261 K
$P_{J,t}/P_\infty$	532	620
Primary jet mass flow	0.116 kg/s[a]	0.117 kg/s[a]
Primary jet thrust	37.5 N[a]	37.9 N[a]
Secondary jet mass flow	0.0013 kg/s[a]	0.0013 kg/s[a]
Secondary jet thrust	0.427 N[a]	0.432 N[a]

[a]These values are for a discharge coefficient of 0.75 for both the primary and secondary nozzles.

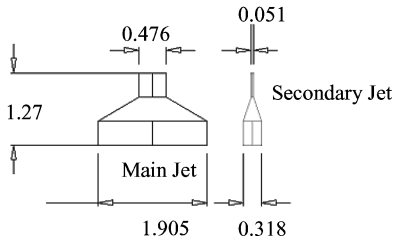

Fig. 3 Primary and secondary jet dimensions (all dimensions in centimeters).

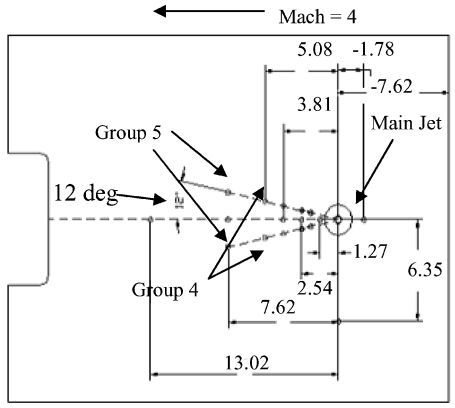

Fig. 4 Top view of the flat plate used in the experiments (all dimensions in centimeters).

the PSP results. The first is due to the camera being mounted on one side of the tunnel, giving a skewed view of the painted surface. Software from Innovative Scientific Solutions, Inc. (OMD version 2.5), helped to compensate for this skewness, giving a more spanwise, symmetric result. The differences between the PSP measurements and the pressure taps are assumed to be a bias error. Finally, the measurement of the pixel size introduced uncertainty into these experiments. By consideration of the contributions of these three sources of error, an uncertainty of 11% in the force and moment results is estimated.

Spark schlieren photographs were taken to visualize and help understand the interaction between the major features in the flow, particularly those of the boundary layer and the main jet and that of the main and secondary jets. The light source for the schlieren photographs was a nanopulser with a time of about 10 ns.

Description of the Computations

The governing equations of a turbulent flow can be written with time-averaged (Reynolds averaged, indicated by an overbar) values of the density and pressure and mass-weighted (Favre averaged, indicated by a tilde) averages for the velocity components and temperature.

Conservation of mass:

$$\frac{\partial \bar{\rho}}{\partial t} + \frac{\partial(\bar{\rho}u_i)}{\partial x_i} = 0 \tag{1}$$

Conservation of momentum:

$$\frac{\partial \bar{\rho}\tilde{u}_i}{\partial t} + \frac{\partial}{\partial x_i}(\bar{\rho}\tilde{u}_i\tilde{u}_i + \bar{p}\delta_{ij}) = \frac{\partial}{\partial x_i}(\tilde{\tau}_{ij} + \bar{\tau}''_{ij}) - \frac{\partial}{\partial x_i}(\bar{\rho}\widetilde{u''_i u''_j}) \tag{2}$$

Conservation of energy:

$$\frac{\partial \bar{\rho}\tilde{e}_0}{\partial t} + \frac{\partial}{\partial x_i}(\bar{\rho}\tilde{e}_0\tilde{u}_i + \overline{pu_i} + \bar{\rho}\widetilde{e''_0 u''_i}) = \frac{\partial}{\partial x_i}(\overline{\tau_{ij}u_j}) - \frac{\partial q''_i}{\partial x_i} \tag{3}$$

where

$$\tilde{e}_0 = \bar{C}_v\tilde{T} + \tfrac{1}{2}\tilde{u}_i\tilde{u}_i + \tfrac{1}{2}\widetilde{u''_i u''_i} \tag{4}$$

The perfect-gas law is used to close the system:

$$\bar{p} = \bar{\rho}R\tilde{T} \tag{5}$$

The Reynolds stress tensor is defined as

$$\tau_{ij} = -\bar{\rho}\widetilde{u''_i u''_j} \tag{6}$$

First-order models, also known as turbulent viscosity models, make use of the Boussinesq assumption:

$$-\bar{\rho}\widetilde{u''_i u''_j} = \mu_T\left(\frac{\partial \tilde{u}_i}{\partial x_j} + \frac{\partial \tilde{u}_j}{\partial x_i} - \frac{2}{3}\delta_{ij}\frac{\partial \tilde{u}_k}{\partial x_k}\right) - \frac{2}{3}\delta_{ij}\bar{\rho}k \tag{7}$$

where μ_T is the turbulent viscosity and k is the kinetic energy of the turbulent fluctuations. All of the numerical calculations performed in this study used Wilcox's k–ω turbulence model.[10,11] This model was chosen because of its good capability in the prediction of separation and in dealing with adverse pressure gradients and separated flows compared to other two-equation models.[11,12] The following equations are used in Wilcox's k–ω turbulence model to close the system of the governing equations.

Eddy viscosity:

$$\mu_T = C_\mu(\bar{\rho}k/\omega) \tag{8}$$

Turbulent kinetic energy equation:

$$\rho\frac{\partial k}{\partial t} + \rho U_j\frac{\partial k}{\partial x_j} = \tau_{ij}\frac{\partial U_i}{\partial x_j} - \beta^*\rho k\omega + \frac{\partial}{\partial x_j}\left[\left(\mu + \sigma^*\mu_T\right)\frac{\partial k}{\partial x_j}\right] \tag{9}$$

Specific dissipation rate equation:

$$\rho\frac{\partial \omega}{\partial t} + \rho U_j\frac{\partial \omega}{\partial x_j} = \alpha\frac{\omega}{k}\tau_{ij}\frac{\partial U_i}{\partial x_j} - \beta\rho\omega^2 + \frac{\partial}{\partial x_j}\left[(\mu + \sigma\mu_T)\frac{\partial \omega}{\partial x_j}\right] \tag{10}$$

The empirical closure coefficients for the 1988 model are

$$\alpha = 5/9, \qquad \beta = 3/40, \qquad \beta^* = 9/100, \qquad \sigma = \sigma^* = 1/2$$

The numerical solver used in this study is AeroSoft's structured flow solver GASP, version 4.0. GASP was chosen because it is a mature program with a proven reliability record in simulations of turbulent flows,[13] vortical flows,[14] jets,[15] shock–vortex interaction,[16] and jet-interaction flows.[17] GASP solves the integral form of the time-dependent Reynolds-averaged Navier–Stokes (RANS) equations in three dimensions.[18,19]

The solution was driven to a steady-state by the use of the implicit Gauss–Seidel scheme. The inviscid fluxes were computed in three dimensions by the use of the flux-vector splitting of Roe and had third-order spatial upwind biased accuracy with the min–mod limiter. The viscous terms are discretized with a standard second-order accurate central differencing scheme. An exception to this flux

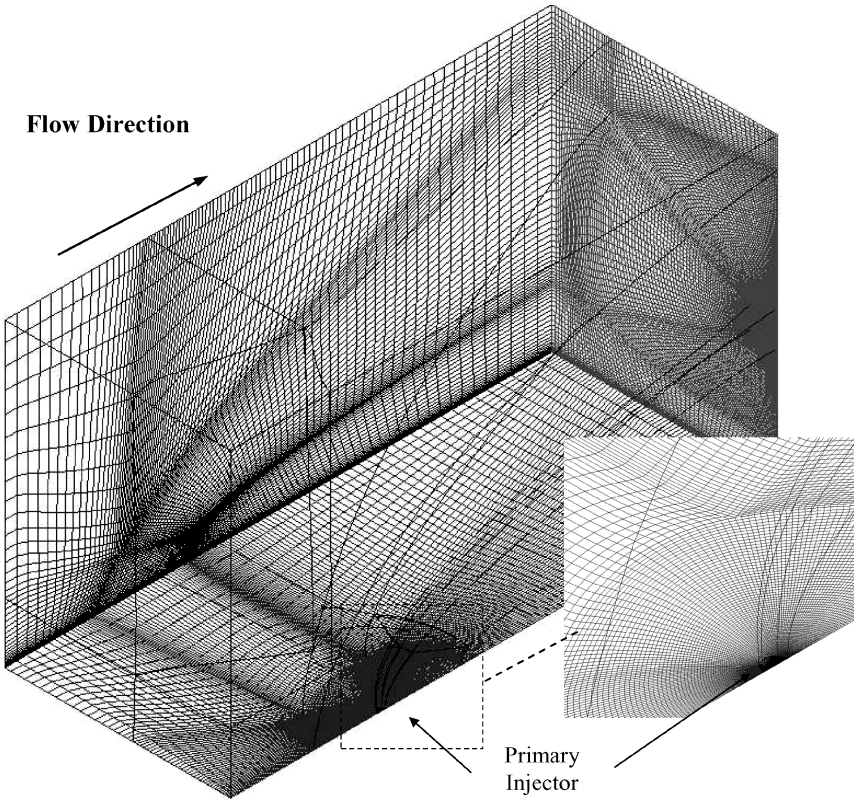

Fig. 5 Isometric view of the computational grid. Insert shows the C-type grid wrapping around the primary injector.

combination was the replacement in only one computational direction of the Roe flux with the Van Leer flux, leaving all of the other parameters unchanged to avoid the carbuncle effect (see Ref. 20).

The grid design used in this work is a combination of H- and C-type grids shown in Fig. 5 that allows a near-optimal cell clustering near the injector. The grid size was dictated by the need to find a balance between the grid refinement and the time to converge a solution to a steady state.

The secondary injector was simulated by the use of a chimera grid that substituted a block of the original computational domain. The chimera grid was considerably finer than the original block it replaced (179,564 vs 814,044 cells) because one of the goals of the substitution was to better resolve the flow details in the region around the secondary injector and perform a localized grid convergence study. The overall size of the grid with the chimera block is 2,073,024 cells compared to 1,544,098 for the baseline grid. The localized grid convergence study of the mesh around the secondary injectors demonstrated that the fine chimera grid produced a converged flowfield solution in the region around the secondary injector.[21]

All grids were created with GRIDGEN version 13.3 (Ref. 22). Care was taken to ensure that the cells closest to the solid surface would lie below a y^+ of 1.0. One-dimensional hyperbolic tangent stretching[23] was used in all regions to distribute the cells along the grid connectors. The injector was simulated by cells on the surface of the flat plate with imposed pressure and velocity equal to the jet total conditions. The grid was sequenced twice by elimination of every other cell in the three spatial directions. Note that, according to the coordinate axis used to define the computational domain in this study, a negative pitching moment about the center of the primary jet indicates a nose-down moment. On average, it would take 2090 total CPU hours with SGI Origin CPUs to converge a turbulent calculation on a 1.5-million-cell grid.

The computational domain for the flat plate with normal injection consisted of a six-sided box (Fig. 5). The lower plane, that is, the plane defined by $y/d = 0.0$, corresponds to the solid surface of the flat plate. The no-slip condition ($u = v = w = 0.0$) is imposed on the flat plate, along with $\partial p/\partial y = 0.0$ and the adiabatic wall condition $\partial T/\partial y = 0.0$. The injector is cut into the surface of the flat plate, and sonic conditions were applied at the cells simulating the jet ($M_J = 1.00$, $\rho_J = \rho^*$, $u_J = w_J = 0.0$ m/s, $v_J = v^*$, and $p_J = p^*$). The jet was assumed to have a step profile, that is, no boundary-layer profile, in the nozzle that was simulated. The area of the simulated jet is smaller than the real jet, and the ratio of the two areas is equal to the discharge coefficient Cd_J of the real nozzle. In this way, the viscous effects inside the nozzle were taken into consideration, and the mass flow of the simulated jet was the same as the real jet. The secondary injectors are cut into the surface of the flat plate, and the same total conditions as the primary jet are applied to them. The flow upstream of the injector is supersonic, and a turbulent boundary layer is present. All of the dependent variables on the entry plane outside the boundary layer were assigned their respective freestream value. The initial freestream turbulence intensity (TI) was assumed to be 5% because no turbulence measurements were available. This value was thought to be a reasonable assumption, given the tunnel conditions. In general, given Wilcox's k–ω sensitivity to the freestream conditions (see Ref. 24), the forces and moments on the flat plate might have been affected when the inlet turbulence level was fixed. However, only the initial inlet turbulence level was specified. That is, the inlet TI was fixed only during the very first iteration, and then the inlet turbulence level was extrapolated from the interior turbulence quantities. In this way, the inlet turbulence intensity was not fixed and could adjust and relax to the proper level. In light of this approach, the final solution should not be sensibly affected by the initial freestream TI. Note that, due to restrictions in computational resources, a sensitivity analysis of forces and moments to the initial freestream TI was not performed. The entry boundary-layer thickness δ was obtained from the schlieren photographs of the tunnel flow, and the boundary-layer velocity profile was assumed to follow the one-seventh power law relationship.

The symmetry plane is represented by the x–y plane. The three remaining sides of the computational domain (the exit plane, the top surface, and the longitudinal plane opposite the symmetry plane) do not represent any physical surface. The top surface and the sidewall of the wind tunnels were assumed[4–6] or actually measured[7] to be distant enough from the injector not to interfere with the flowfield of interest. Therefore, a first-order extrapolation boundary condition

was applied to these surfaces, as well as to the downstream exit plane.

The iterative convergence of the calculations was determined by verification of the variation over time of several flow parameters. Convergence was declared when the normal force, axial force, and pitching moment were steady. The discretization error of the computations was calculated with the "Mixed 1st + 2nd Order Richardson Extrapolation" described by Roache[25] because, according to Roy,[26] this method "produces the best error estimation for non-monotonic, mixed-order solutions." The procedure made use of the solution and of the ratio of the number of cells on the three grid sequences to estimate the discretization error on the fine grid sequence. The discretization error on the fine grid was estimated to be 0 and 1% for the normal force and 4 and 21% for the pitching moment for the case with only the primary injector and the case with the primary injector plus group 1 jets, respectively. Complete details of the computations and of the estimation of the uncertainty can be found in Refs. 21 and 27.

Experimental Results

The results are presented mainly as comparisons between the surface pressure field (a ratio of the local surface pressure to the freestream static pressure) created by the primary injector only case (top half of Figs. 6–8) and different jet configurations (bottom half of Figs. 6–8). A horizontal line separates the results for the two cases. Figures 6–8 show the cases with a pressure ratio of 620. The flow direction is from left to right. The main injector is shown as a black circle at $X = 0$ and $Y = 0$. The group 1 secondary injector can be seen as a small black dot at approximately $X = 1.778$ cm, $Y = 0.51$ cm, and the other secondary jets can be seen farther downstream. A high-pressure region, as expected, can be observed upstream of the primary injector in all of the cases.

Consider the surface pressure comparison of the primary jet only case and the primary plus group 1 and 2 secondary jets case shown in Fig. 6. Note that upstream and downstream for the secondary jets are not simply left and right on the graph because they are experiencing an approaching flow with a large spanwise component caused by the primary jet. Figure 6 shows that the addition of the first two pairs of secondary injectors both increases the size and intensity of the upstream high-pressure region and allows the flow to return to freestream static pressure faster downstream. The low-pressure region is not only reduced in size, but also in intensity.

The effects of adding additional secondary jets can be noted in Figs. 6–8. Figures 6–8 show a successive increase in the positive

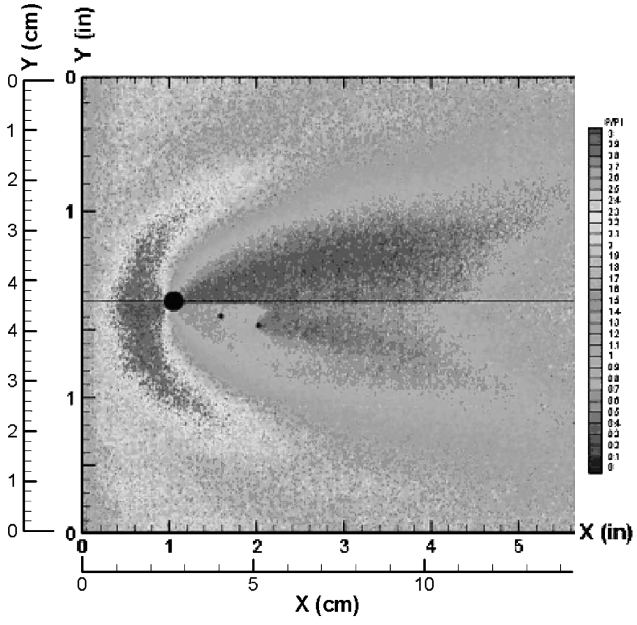

Fig. 6 Surface pressure ratio comparison: $M = 4.0$, $P_0 \sim 10.34$ atm, $P_{0j} = 37.84$ atm, and PR = 620; primary only (top) vs primary + groups 1 and 2 (bottom).

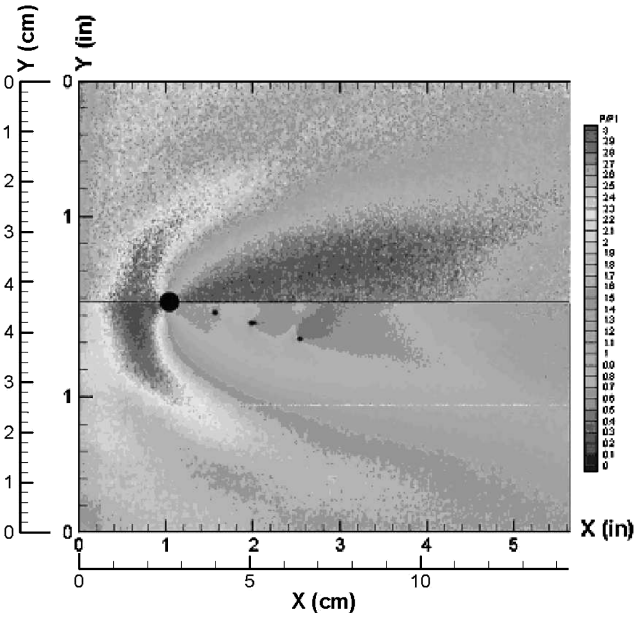

Fig. 7 Surface pressure ratio comparison: $M = 4.0$, $P_0 \sim 10.34$ atm, $P_{0j} = 37.84$ atm, and PR = 620; primary only (top) vs primary + groups 1–3 (bottom).

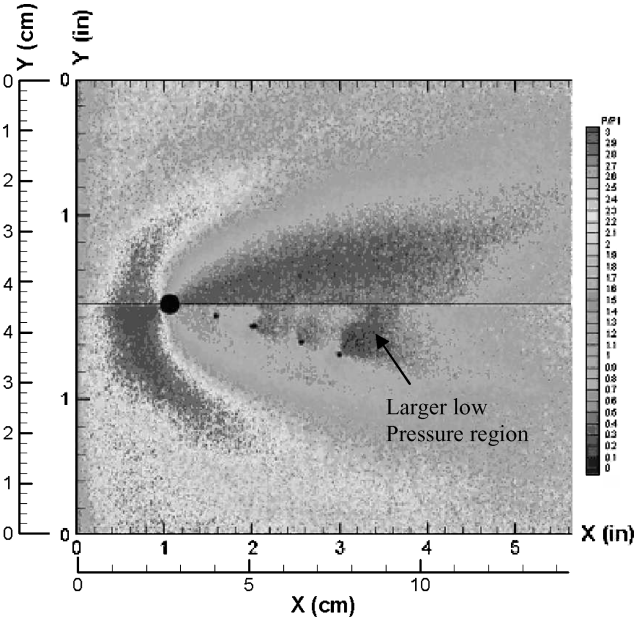

Fig. 8 Surface pressure ratio comparison: $M = 4.0$, $P_0 \sim 10.34$ atm, $P_{0j} = 37.84$ atm, and PR = 620; primary only (top) vs primary + groups 1–4 (bottom).

effects on the surface as more groups of secondary jets are added. When compared with the results of Fig. 6, the primary plus group 1–3 secondary jets case in Fig. 7 shows even more effectiveness in reducing the size and intensity of the downstream low-pressure region. The secondary jets create more high-pressure regions downstream with the same beneficial moment effect. Indeed, the whole low-pressure region is markedly reduced in both size and intensity. The upstream high-pressure region is increased further by the addition of the third pair of injectors. The addition of the fourth pair of secondary injectors, however, begins to show some drawbacks, as demonstrated in Fig. 8. The low-pressure region downstream of the fourth pair of injectors has a much lower pressure than that of the other three pairs. Also, the flow seems to take longer to recover in the primary plus group 1–4 secondary jets case than in the primary plus group 1–3 secondary jets case. The upstream high-pressure

Table 4 Experimental interaction force and moment comparison: $M = 4.0$ and PR = 620[a]

Case	C_{Fy}	ΔC_{Fy}, %	C_{Mz}	ΔC_{Mz}, %
Primary jet only	9.47	0	16,346	0
Primary jet plus group 1, 2 jets	15.29	62	10,094	−38
Primary jet plus group 1–3 jets	16.26	72	11,969	−27
Primary jet plus group 1–4 jets	18.08	91	21,880	34

[a]Results are only for the limited area of the surface that could be observed in the first experimental setup; the contribution of the jet thrust is not included, experimental uncertainty for both the normal force and the pitching moment coefficients was estimated to be ±11%.

region is greatly enlarged. Both of these phenomena would tend to increase the nose-down moment on the plate. Therefore, it is expected that the force on the plate would be increased, but there will be an increased nose-down moment, which is undesirable.

The measurement area for the PSP pressure results was used to detail the integrated effects of the secondary jets on the flowfield of the primary jet. Thus, these data cannot be used to assess the total force and moment corresponding to the complete interaction flowfield. Nevertheless, integrations over the available areas of the surface were made to permit quantitative assessment of the effects of the secondary jets on the interaction forces and moment (thrust of the jet not included) on those limited areas of the surface. The results can be seen in Table 4. The force increases measurably with the addition of successive groups of secondary jets. The primary plus group 1–2 secondary jets case, for example, shows a 62% increase over the primary jet only case. It is evident that the large increase in force is not only due to the increased intensity of the upstream high-pressure region, but also to the reduction in intensity of the downstream low-pressure region. Therefore, the nose-down moment is expected to be reduced, and Table 4 reports this reduction as 38% of the primary jet only value. This is the first case to show both increased force from the jet and decreased nose-down moment. In fact, for the primary plus group 1–3 secondary jets case, the force is increased by 72%, an improvement over the primary plus group 1–2 secondary jets case. However, the reduction in the nose-down moment is decreased from 38 to 27%. This results hints that a point of diminishing returns is being approached with the addition of each pair of jets. This premise is supported by primary plus group 1–4 secondary jets case where the large increase in force (91%) is offset by an increase of nose-down moment (34%).

Numerical Results

A second series of experiments was attempted with a different viewing arrangement intended to capture more of the interaction flowfield upstream of the primary jet. Some of the downstream region was lost, and the viewing area was not a simple rectangle. Furthermore, the pressure ratio (PR) was reduced somewhat to PR = 532. The numerical studies were directed at these cases. Unfortunately, we experienced difficulties with some of the experimental tests in this series, and only the tests with the primary jet alone are considered reliable. Therefore, the comparison of the experimental and computational flowfield is performed only for the case with the primary jet and a pressure ratio of 532. However, the comparison of the measured and predicted augmentation factors compares the trends observed in the experiments with a pressure ratio of 620 with the trends predicted by the computational fluid dynamics (CFD) computations that use PR = 532.

Two injection configurations were simulated by the Mach 4.0, PR = 532 calculations: 1) primary jet only and 2) primary jet plus group 2 secondary jets.

Consider first the case with the primary jet alone. The integrated forces and moments obtained from the numerical solution for the same integration area are compared to the experimental values in Table 5. Note that these values were obtained by integration of the pressure field acting on the flat surface and do not include the thrust contribution from the jets. The CFD solution underpredicted both the normal force and the pitching moment. The numerical results

Table 5 Comparison of experiment to the CFD prediction for force and moment for the VT case with only the primary jet: $M = 4.0$ and PR = 532[a]

Method	C_{Fy}	C_{Mz}	ΔC_{Mz}, %	ΔC_{Mz}, %
Experimental	1.53	−0.87	——	——
CFD	1.16	−0.53	−24	−39

[a]Results are for the limited area of the surface that could be observed in the second experimental setup.

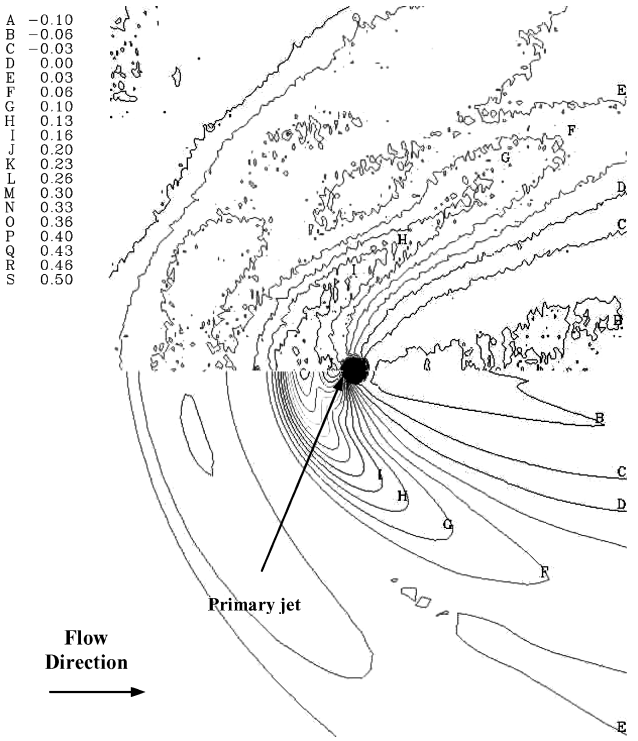

Fig. 9 Comparison of the experimental (top) and numerical (bottom) C_p mappings on the surface of the flat plate: $M = 4.0$ and PR = 532.

underpredicted the normal force by 24%, whereas they underpredicted the pitching moment by 39%. Note that, as mentioned earlier, the main source of the relatively large discrepancies between the measured and computed forces and moments is attributable to two main factors: the difference in pressure ratios used in the experiment (620) and in the CFD (532), and the presence of a shock ahead of the working section of the wind tunnel. (See "Description of the Experiment.") However, it is still possible to conduct an analysis of the trends in the forces and moments and to determine those flowfields features that determine the under/over-prediction in the computations. Look at the comparisons of the numerical and experimental pressure mappings of Fig. 9 and the pressure plots of Fig. 10. The predicted mappings for the case with only the primary jet are in good agreement with the experiment (Fig. 9), the isobars having the same shape and the same values. However, the CFD predicts a higher pressure coefficient in the separation region as shown by the C_p plot of Fig. 10. From Fig. 10, it is also clear that the experimental data does not show the two peaks and the trough in C_p just ahead of the injector. Apart from this discrepancy, the experimental and predicted C_p plots are very similar in the separation region ahead of the injector and in the region of negative pressure aft of the jet.

The experimental C_p mapping shows considerably more noise than the CFD, as indicated by the jagged isobars of the top half of Fig. 10. It is not possible to assess exactly whether the separation location is properly predicted by the CFD because the experimental data do not extend upstream far enough. From the C_p plot in Fig. 10, it seems that the CFD slightly underpredicts the separation location. The predicted larger separation region and higher C_p just ahead of the primary injector explains why the CFD pitching

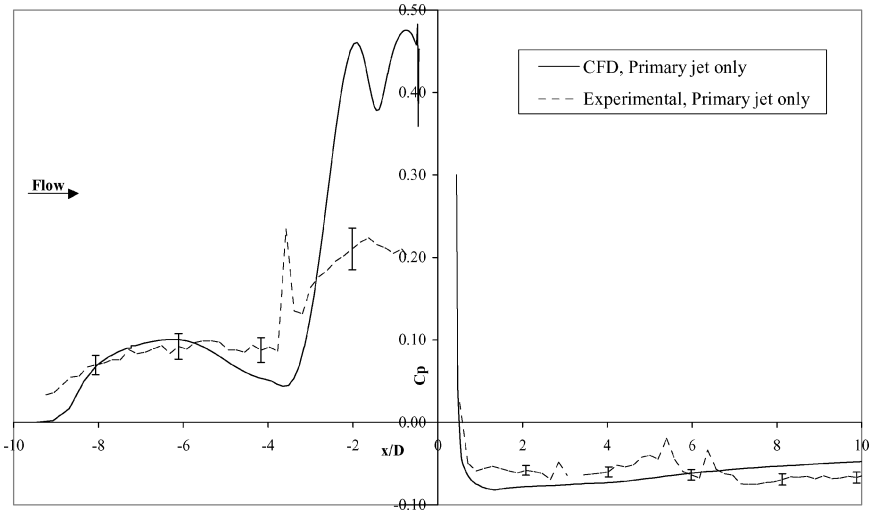

Fig. 10 Pressure coefficient plots between ——, the numerical solution and - - - -, the experiment, with error bars: $M = 4.0$ and PR = 532.

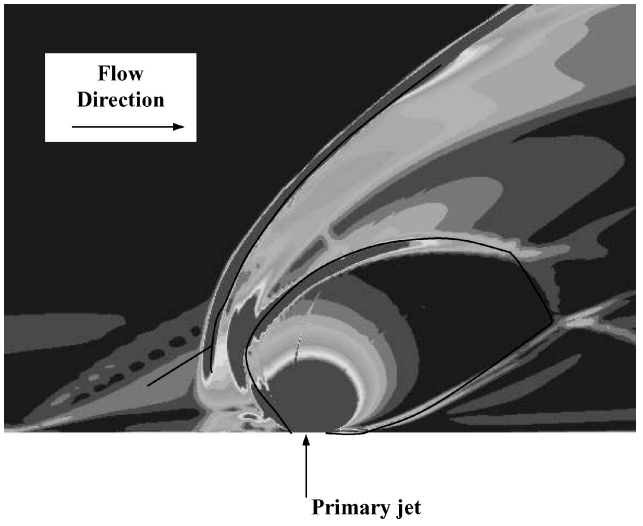

Fig. 11 Comparison of the schlieren photographs with the CFD solution on the plane of symmetry (CFD contours represent spatial derivative of density; compare Fig. 2.)

moment is less negative by 39% than the experimental value (Table 5). In fact, a force pushing down on the plate at a location ahead of the primary injector produces a positive (nose-down) moment.

The schlieren photograph of Fig. 2 provides a means to draw an outline of the main flow features visible in the experiment such as the barrel shock, the bow shock, and the separation-induced shock. Because schlieren photographs depict the first spatial derivative of the density, the outline of the flow features drawn from these photographs can be superimposed on the mapping of this parameter on the plane of symmetry produced by the numerical solution. Note that although the schlieren photograph is a two-dimensional representation of a three-dimensional flow, the CFD solution shown is a real two-dimensional slice through the three-dimensional flowfield. Therefore, some of the flow features visible in the schlieren photographs that may appear to lie on the symmetry plane do not lie on it in actuality and cannot be compared to the CFD mappings on the symmetry plane. The visual comparisons of the schlieren photograph to the numerical solution are shown in Fig. 11. The CFD correctly predicted the location of the separation-induced shock (at least near the location where it impinges on the bow shock) and the location and shape of the bow shock and barrel shocks.

The comparison with the experiment presented an uncertainty due to the presence of a shock ahead of the tunnel working section produced by misalignment of the junction of the tunnel floor with

Table 6 Predicted increase in normal force and pitching moment due to the action of the secondary jets, without consideration of the thrust of the jets or uncertainties calculated with the mixed first- and second-order Richardson extrapolation[25]: $M = 4.0$ and PR = 532

Case	C_{Fy}	ΔC_{Fy}, %	C_{Mz}	ΔC_{Mz}, %
Primary jet only	$1.16_{\pm 0\%}$	0.0	$-0.53_{\pm 4\%}$	0.0
Primary jet plus group 1 secondary jets	$1.19_{\pm 1\%}$	2.9	$-1.40_{\pm 21\%}$	164

the flat plate (Fig. 2). Therefore, it is convenient to compare the force and moment augmentation factor of the secondary jets rather than to compare directly the experimental and numerical forces and moments. The force and moment increase generated by the primary plus group 1 secondary injectors are listed in Table 6. According to the numerical solution, the normal force is increased by 2.9%, whereas the pitching moment is made more negative (nose-up) by 164%, that is, the nose-down attitude of typical jet interaction configurations is decreased. This result is very important because it clearly indicates that the secondary jets alleviate the nose-down moment created by the primary injector as intended.

The increase in the normal force and the decrease in the nose-down pitching moment can be understood from the pressure coefficient mapping in Fig. 12. The upper half of Fig. 12 shows the results with only the primary injector and the lower part with group 2 secondary injectors activated. The secondary injectors marginally reduce the area of negative C_p behind the primary injector. They also make the separation region extend farther upstream than the case with only the primary jet. However, the C_p in the two separation lobes does not reach the high levels seen in the single-jet case. This phenomenon is visible in the C_p plot along the tunnel centerline of Fig. 13. Note the complex shape of the zero-C_p line (line D) for the case with only the primary jet (Fig. 12, top half). In other experimental cases, for example, Refs. 5 and 6, the zero-C_p line appeared to radiate almost linearly from the region of the primary injector toward the downstream location. However, in this case, the zero-C_p line extends linearly up to a certain downstream location and then it moves back upstream to form a lobe around a region of higher pressure (line E in top half of Fig. 12). Note that when the secondary injectors were activated, the lobe formed by the zero-C_p line around the higher-pressure region was canceled by the effects of the secondary injectors.

The effects of the secondary jets on the computed pressure distribution along the centerline are shown in Fig. 13. The separation region in the case with the secondary jets appears larger than the case with only the primary injector, even though the peak pressures are lower. The secondary injectors also affect the region aft of the

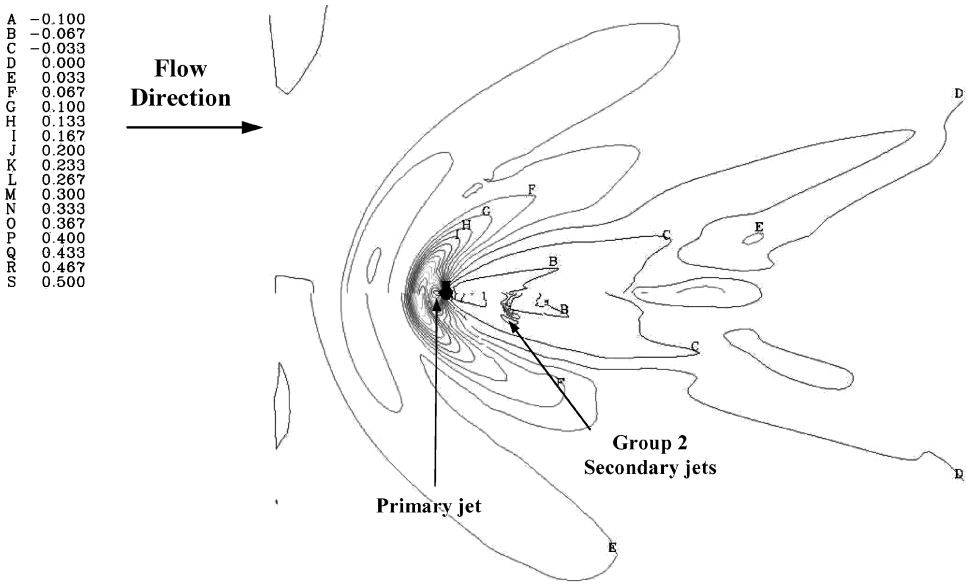

Fig. 12 Comparison of the CFD C_p results for the primary jet only case (top) and the primary jet plus 1 secondary jet case (bottom): $M = 4.0$ and Pr 532.

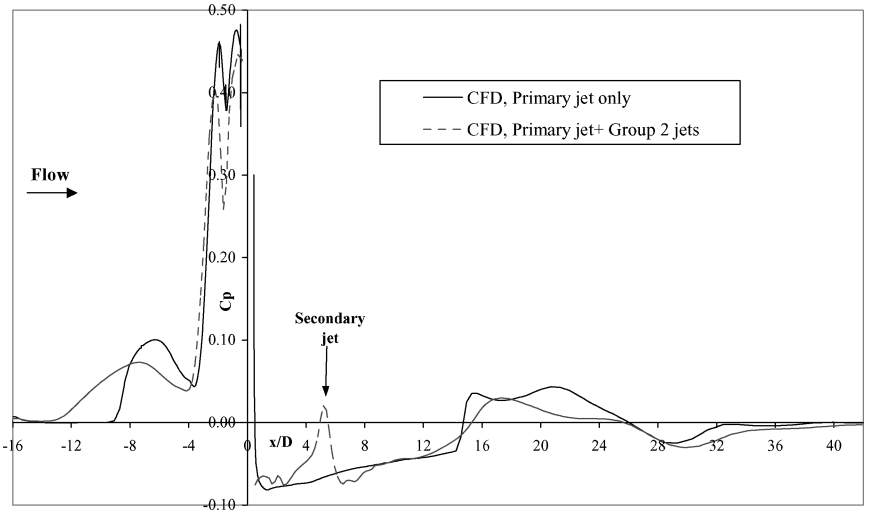

Fig. 13 Comparison of the predicted C_p plots along the tunnel centerline for the primary jet only case: $M = 4.0$ and $Pr = 532$.

primary injector. Note the steep pressure rise in the middle of the region of negative pressure at x/d of 5.0. In addition to this, the secondary injectors smear and push downstream the location at which the reflected shock of the Mach disk impinges on the flat plate from x/d of 15.0 to 17.0. This location is indicated by the steep pressure increase at $x/d \approx 15.0$ for the case with the primary jet only. The weakened reflected shock also does not thicken the boundary layer as much as in the case of the primary jet alone, and the region of positive C_p aft of the impingement is shorter. The weakening of the reflected shock is a consequence of the secondary injector impinging on the back side of the barrel shock, in this way reducing the size of the barrel shock itself. Because of this mechanism, the injectant does not expand to such a large extent inside the barrel shock as in the primary jet alone case, and the Mach disk has virtually disappeared from the top of the barrel shock. Also, the wake behind the plume is larger when the secondary injectors are activated, which indicates a slower mixing between the injectant and the freestream fluid. These differences, such as the larger separation and the lack of a strong reflected shock for the case with the secondary injectors, are confirmed by the mappings of the Mach number contours on the plane of symmetry in Fig. 14. The top half of Fig. 14 shows the Mach contours for the case with only the primary jet, whereas the bottom half shows the Mach contours for the case with the primary jet and group 2 jets. Note how the Mach disk disappears from the top of the barrel shock generated by the primary jet when the secondary injectors are activated. Also note the larger size of the separation region and the lack of the reflected shock impinging on the flat plate when the secondary jets are activated.

A better understanding of the physics of the flowfield can be obtained by a study of the isometric plotting of the streamlines and of the contours of Fig. 15. This flowfield snapshot shows the Mach contours mapped on the plane of symmetry, the C_p contours mapped on the surface of the flat plate and the vorticity magnitude contours mapped on the crossplane aft of the barrel shock. The paths of the trailing vortices are highlighted by streamlines that follow the vortex core. The horseshoe vortex is created in the separation region by one of a couple of counter-rotating vortices,[21,28] and trails downstream and away from the plane of symmetry. The second counter-rotating vortex in the separation region forms the upper trailing vortex that follows the upstream edge of the barrel shock and slowly moves away from the plane of symmetry. A complex system of vortices forms at the Mach disk (vortex 1) and along the barrel shock (vortex 2) at the location where the reflected shock inside the barrel shock creates a sharp angle of the barrel itself. These primary vortices trail downstream in a direction parallel to the plane of symmetry, and they

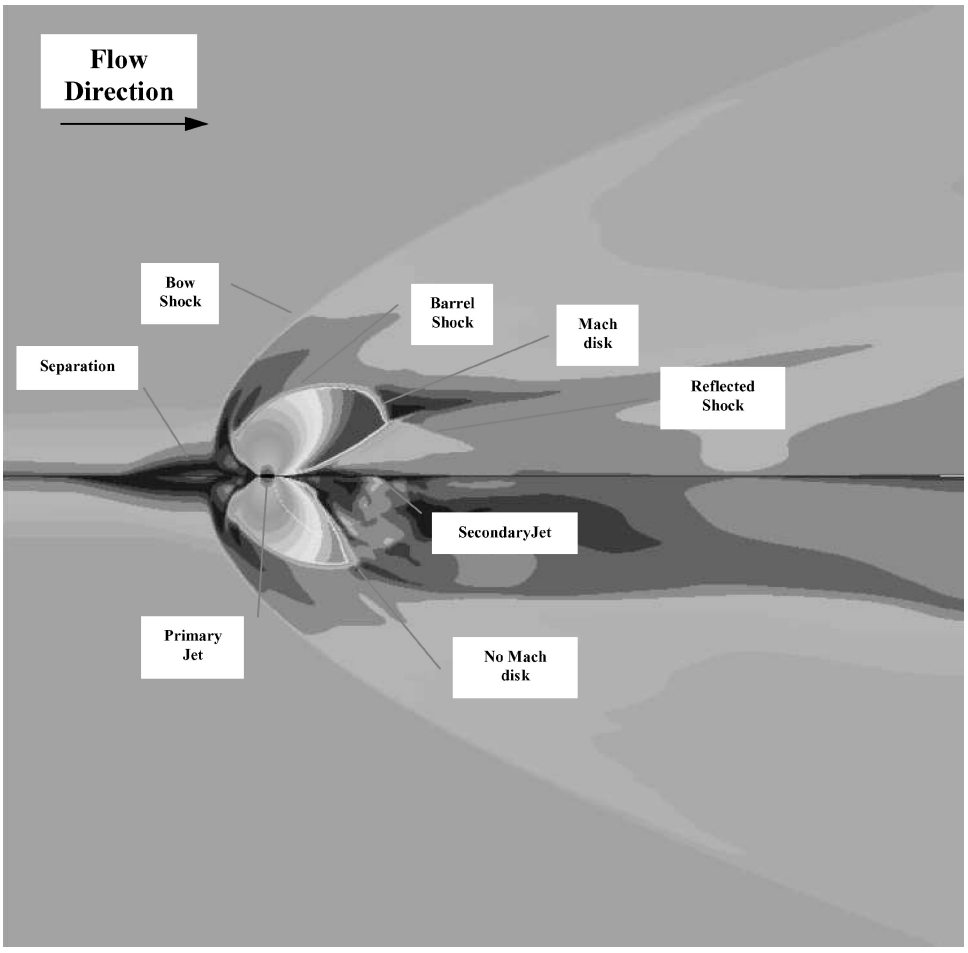

Fig. 14 Comparison of the CFD Mach contours on the plane of symmetry for the primary jet only case (top) and the primary jet plus 1 secondary jet case (bottom): $M = 4.0$ and $Pr = 532$.

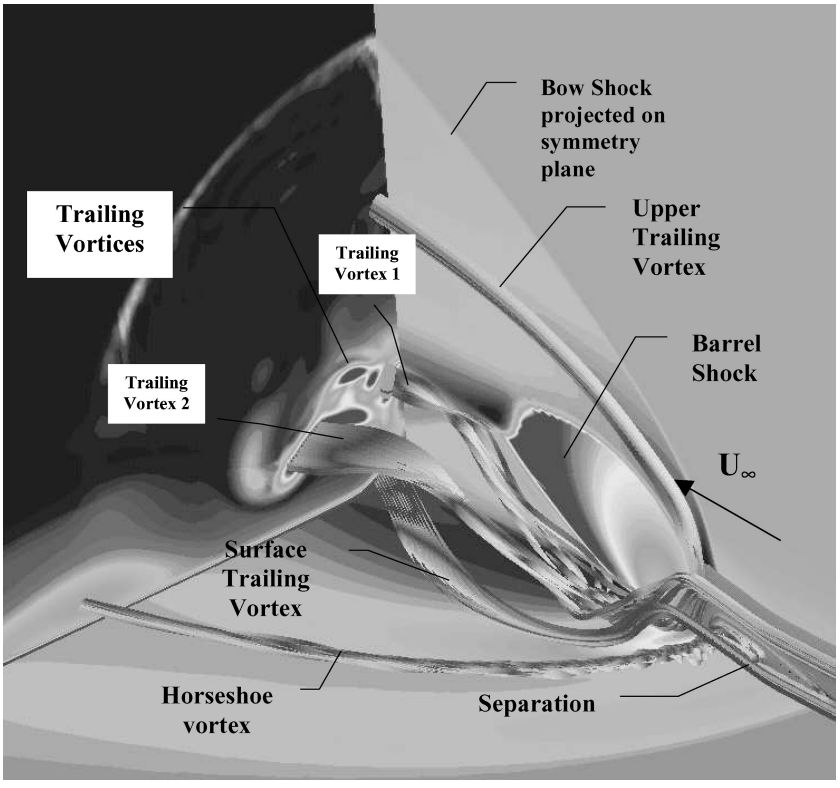

Fig. 15 Isometric view of the oblique barrel shock with streamlines identifying the main rotational motion (Mach number contours on symmetry plane, C_p contours on surface of flat plate, vorticity magnitude contours on crossplane): $M = 4.0$ and $Pr = 532$, primary jet only.

tend to merge into one large vortical system as they are convected downstream. Finally, the surface trailing vortex forms at the upstream edge of the barrel shock (Fig. 15), and, to be convected around the footprint of the barrel shock, it moves away from the symmetry plane as the barrel shock expands. Once the axis of the injector has been passed at $x/d = 0.0$ and the barrel shock detaches from the surface of the flat plate, the vortex moves back toward the centerline and into the low-pressure region behind the injector. Because of its closeness to the solid surface, the trailing vortex entrains large quantities of boundary-layer fluid as it trails downstream.

Conclusions

This combined experimental–numerical study showed that it is possible to improve present-day jet thruster configurations for supersonic crossflows and high jet pressure ratios by the use of an array of smaller secondary injectors that interact with the primary jet. It was shown that the main improvement of this configuration is a considerable reduction in the nose-down pitching moment typical of jet-interaction flows. A secondary benefit is a small increase in the normal force. These two effects were found to be caused by the reduction in both size and intensity of the low-pressure region aft of the primary injector and, in some cases, by an increase in the extent and intensity of the upstream separation region. However, the location of the array of the secondary injectors was not optimized here, and it is believed that even larger improvements in the performance can be obtained by strategic location of the secondary injectors. The investigation further demonstrated that a combined effort of numerical studies and experiments could efficiently and effectively lead to the understanding of complex fluid-dynamics phenomena. Such a coordinated approach is most desirable in the development and design stages of new technologies because of its time- and cost-saving advantages over an exclusively experimental or numerical approach.

The RANS equations, in conjunction with a first-order two-equation turbulence model such as Wilcox's k–ω, were shown to be able to reproduce the main physics of a highly complex phenomenon such as the multiple jet interaction flowfield. The k–ω turbulence model proved to be reliable and robust, and the results it provided for this type of flowfield were accurate enough from an engineering standpoint. However, in spite of the overall good performance, the k–ω turbulence model failed to predict correctly the flow in the regions of strong adverse pressure gradients. Comparisons with experimental results showed that the separation region was often underpredicted, highlighting the need to employ second-order turbulence models for more accurate results.

A large effort was dedicated to the development of an efficient computational grid that could capture the flow physics with the least amount of cells. The grid was adapted to the physics of the flow via a combination of H- and C-type grids. Also, chimera or overset grids were employed in the simulation of the secondary injectors to improve the efficiency of the calculation.

The numerical solutions made possible a detailed study of the three-dimensional jet-interaction flowfield. The analysis showed that the primary mechanism responsible for the creation of the jet-interaction pressure field is the interaction of strong vortical structures with the bow-barrel shock systems.

References

[1]"Computational and Experimental Assessment of Jets in Crossflow," *Proceedings of the 72nd AGARD Fluid Dynamics Panel Meeting and Symposium*, CP 534, AGARD, 1993.

[2]Spaid, F. W., Zukoski, E. E., and Rosen, R., "A Study of Secondary Injection of Gases into a Supersonic Flow," NACA TR 32-834, Aug. 1966.

[3]Schetz, J. A., Cox-Stouffer, S., and Fuller, R., "Integrated CFD and Experimental Studies of Complex Injectors in Supersonic Flows," AIAA Paper 98-2780, June 1998.

[4]Schetz, J. A., Hawkins, P. F., and Lehman, H., "Structure of Highly Underexpanded Transverse Jets in a Supersonic Stream," *AIAA Journal*, Vol. 5, No. 5, 1967, pp. 882–884.

[5]Cubbison, R. B., Anderson, B. H., and Ward, J. J., "Surface Pressure Distributions with a Sonic Jet Normal to Adjacent Flat Surfaces at Mach 2.92 to 6.4," NASA TN D-580, 1961.

[6]Letko, W., "Loads Induced on a Flat Plate at a Mach Number of 4.5 with a Sonic or Supersonic Jet Exhausting Normal to the Surface," NASA TN D-1935, 1963.

[7]Wallis, S., "Innovative Transverse Jet Interaction Arrangements in Supersonic Crossflow," M.S. Thesis, Dept. of Aerospace and Ocean Engineering, Virginia Polytechnic Inst. and State Univ., Blacksburg, VA, Dec. 2001.

[8]Morris, M., and Donovan, J., "Application of Pressure and Temperature Sensitive Paints to High Speed Flows," AIAA Paper 94-2231, June 1994.

[9]Crites, R. C., "Pressure Sensitive Paint Technique," Von Kármán Inst. for Fluid Dynamics, Lecture Series 1993-05, *Measurement Techniques*, April 1993.

[10]Wilcox, D. C., *Turbulence Modeling for CFD*, 2nd ed., DCW Industries, Inc., La Cañada, CA, 1998.

[11]Wilcox, D. C., "Comparison of Two-Equation Turbulence Models for Boundary Layers with Pressure Gradient," *AIAA Journal*, Vol. 38, No. 8, 1993, pp. 1414–1421.

[12]Payne, J. L., Roy, C. J., and Beresh, S. J., "A Comparison of Turbulence Models for a Supersonic Jet in Transonic Cross Flow," AIAA Paper 2001-1048, Jan. 2001.

[13]Roger, R. P., and Chan, S. C., "Parameters Affecting Penetration of a Single Jet into a Supersonic Crossflow: A CFD Study, II," AIAA Paper 98-0425, Jan. 1998.

[14]Nedungadi, A., and Lewis, M. J., "A Numerical Study of Fuel Mixing Enhancement Using Oblique Shock/Vortex Interactions," AIAA Paper 96-2920, July 1996.

[15]Hsieh, T., "Analysis of the Scaling Effects for Missile Configuration with Lateral Thruster," AIAA Paper 99-0810, Jan. 1999.

[16]Nadungadi, A., and Lewis, M. J., "Computational Study of the Flowfields Associated with Oblique Shock Vortex Interactions," *AIAA Journal*, Vol. 34, No. 12, 1996, pp. 2545–2553.

[17]McDaniel, J., Glass, C., Staack, D., and Miller, C., "Experimental and Computational Comparison of an Underexpanded Jet Flowfield," AIAA Paper 2002-0305, Jan. 2002.

[18]*GASP 3.2 User Manual*, AeroSoft, Blacksburg, VA, 1997.

[19]*GASP 4.0 User Manual*, AeroSoft, Blacksburg, VA, 2001.

[20]Peery, K. M., and Imlay, S. T., "Blunt-Body Flow Simulations," AIAA Paper 88-2904, July 1988.

[21]Viti, V., "Numerical Studies of the Jet Interaction Flowfield with a Main Jet and an Array of Smaller Jets," Ph.D. Dissertation, Dept. of Aerospace and Ocean Engineering, Virginia Polytechnic Inst. and State Univ. Blacksburg, VA, Sept. 2002; also URL: http://scholar.lib.vt.edu/theses/ [cited 18 Sept. 2002].

[22]*GRIDGEN Version 13.3 User Manual*, Pointwise, Inc., Bedford, TX, 1999.

[23]Vinokur, M., "On One-Dimensional Stretching Functions for Finite Difference Calculations," *Journal of Computational Physics*, Vol. 50, No. 3, 1983, pp. 215–234.

[24]Bardina, J. E., Huang, P. G., and Coakley, T. J., "Turbulence Modeling Validation, Testing and Development," NASA TM 110446, April 1997.

[25]Roache, P. J., *Verification and Validation in Computational Science and Engineering*, Hermosa, Albuquerque, NM, 1998.

[26]Roy, C. J., "Grid Convergence Error Analysis for Mixed-Order Numerical Schemes," AIAA Paper 2001-2006, June 2001.

[27]Viti, V., Schetz, J., and Neel, R., "Numerical Studies of the Jet Interaction Flowfield with a Main Jet and an Array of Smaller Jets," International Congress of Aeronautical Sciences, ICAS Paper 2002-4.7.1, Sept. 2002.

[28]Chenault, C. F., and Beran, P. S., "K–ε and Reynolds Stress Turbulence Model Comparisons for Two-Dimensional Injection Flows," *AIAA Journal*, Vol. 36, No. 8, 1998, pp. 1401–1412.

W. Dahm
Associate Editor